Nano Research

Open Access

Research Article

Post-assembly covalent programming of colloidal molecules via multivalent N-heterocyclic carbenes

Runshi Qiao[1], Huaining Zha[1], Jing Tao[1], Huibin He[1,2] ✉, Di Zheng[1], Weijia Kong[1], Yilin Bao[1], Xinyue Zhang[1], Xiayun Huang[1], Yutao Sang[1] ✉, and Zhihong Nie[1] ✉

[1] *State Key Laboratory of Molecular Engineering of Polymers, Department of Macromolecular Science, Fudan University, Shanghai 200438, China*

[2] *The Key Laboratory of Functional Molecular Solids, Ministry of Education, and School of Chemistry and Materials Science, Anhui Normal University, Wuhu 214002, China*

Cite this article: *Nano Research*, **2026**, *19*, 94908810. https://doi.org/10.26599/NR.2026.94908810

ABSTRACT: Nanoparticle (NP) assemblies exhibit collective optical, electronic, and magnetic properties that enable applications in sensing, catalysis, energy conversion, and optoelectronics. However, achieving independent control over structural integrity and surface functionality within such assemblies remains a significant challenge in NP self-assembly. Here, we report a modular post-functionalization strategy that decouples structural locking from surface reprogramming in colloidal molecules (CMs). AB_n symmetry CMs assembled from complementary polymer-grafted Au NPs were selected as representative models and reinforced using multivalent N-heterocyclic carbene (NHC)-containing block copolymers. The NHC anchoring segments form robust C–Au bonds, converting initially noncovalent interparticle junctions into covalently bridged connections without perturbing predefined geometries. This multivalent locking reduces interparticle spacing, enhances plasmonic coupling, and significantly improves chemical, ionic, thermal, and mechanical stability, preserving three-dimensional architectures in the dry state. Importantly, separation of anchoring and functional polymer blocks enables independent introduction of amphiphilic and light-responsive surface properties, allowing solvent-dependent plasmonic modulation and reversible light-triggered hierarchical assembly while maintaining discrete CM geometry.

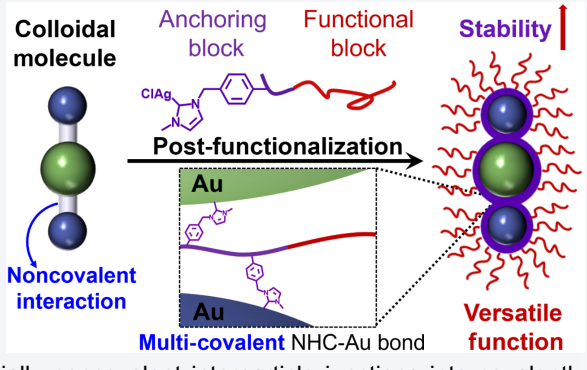

KEYWORDS: nanoparticle self-assembly, colloidal molecules, carbene-containing block polymers, structural stability and amphiphilicity, light-responsiveness

1 Introduction

The self-assembly of nanoparticles (NPs) has emerged as a powerful bottom-up strategy for constructing architected materials with collective properties that are absent in individual building blocks [1–4]. These emergent behaviors originate from interparticle coupling, such as plasmonic, excitonic, or magnetic interactions, and are highly sensitive to the dimensionality, symmetry, orientation, and spatial precision of the assemblies [5]. Over the past two decades, self-assembly approaches have enabled the construction of diverse NP architectures, including colloidal molecules (CMs) [6–8], chain-like superstructures [9–11], vesicular assemblies [12–14], and ordered two- and three-dimensional (3D) superlattices [15–18]. Central to this field is the ability to engineer interparticle interactions with molecular precision. Surface functionalization using small molecules [19, 20], DNA [21], proteins [22], or polymers [23, 24] provides a versatile toolbox for directing assembly pathways. Among these ligands, polymers are particularly attractive because their molecular structure, functionality, chain length, and responsiveness can be readily tailored [25]. Polymer-mediated interactions have enabled programmable assembly into various architectures with applications spanning nanomedicine, catalysis, sensing, energy conversion, and optoelectronics [26].

Despite these advances, polymer-grafted NP assemblies face three fundamental limitations that restrict their practical utility. First, most assemblies rely on weak and reversible noncovalent

Received: March 26, 2026; **Revised:** May 4, 2026
Accepted: May 4, 2026

✉Address correspondence to Huibin He, huibin.he@ahnu.edu.cn; Yutao Sang, sangyt@fudan.edu.cn; Zhihong Nie, znie@fudan.edu.cn

interactions, such as hydrogen bonding [27], electrostatic attraction [28, 29], or hydrophobic effects [30–32], between surface-bound polymer chains [25]. These interactions are intrinsically sensitive to solvent polarity, ionic strength, and temperature, rendering the resulting architectures environmentally fragile. Structures stable in solution frequently undergo collapse, fusion, or rearrangement upon solvent removal or external perturbation [15, 33]. Second, polymer linkers introduce conformational freedom at interparticle junctions. While such flexibility can facilitate assembly formation, it inevitably leads to dynamic fluctuations in interparticle spacing and structural distortion [9, 34]. As a consequence, assemblies often lack mechanical rigidity and geometrical fidelity, which are essential for applications that rely on fixed spatial configurations and well-defined coupling distances. Third, and more fundamentally, ligand design has been predominantly focused on controlling interparticle attraction and repulsion, whereas the surface physicochemical properties of the resulting assemblies have received comparatively little attention [9]. Because interparticle interactions are exquisitely sensitive to subtle variations in ligand architecture, pre-programming surface properties (e.g., amphiphilicity or stimuli-responsiveness) during initial NP functionalization often perturb the delicate balance required for assembly formation. This intrinsic coupling between assembly-driving interactions and surface functionality imposes a critical design constraint: Structural programmability and surface tunability are rarely independently achievable. To address these limitations, several post-assembly stabilization strategies have been developed, such as encapsulating the assemblies within polymer micelles [35, 36] and covalently crosslinking the polymer ligands on NPs [37]. By decoupling structural reinforcement from the assembly process, these approaches simplify interaction design and enhance robustness. However, they primarily aim to improve structural stability and rigidity, and generally do not offer a systematic route to modulate surface physicochemical properties while preserving the pre-formed spatial configuration. Therefore, a general strategy that enables independent control over structural integrity, mechanical rigidity, and surface functionality, without disrupting the programmed assembly architecture, remains an unresolved challenge in NP self-assembly.

Herein, we present a modular post-functionalization strategy that enables independent control over structural integrity and surface functionality in NP assemblies (Fig. 1). AB_n symmetry CMs, assembled from poly(acrylic acid) (PAA)-grafted Au NPs (NP-A) and poly(ethylene glycol) (PEG)/(11-mercaptoundecyl)-*N*,*N*,*N*-trimethylammonium bromide (TMA)-cofunctionalized Au NPs (NP-B), were selected as representative models owing to their geometrically well-defined architectures (Fig. 1(a)). To achieve covalent reinforcement, block copolymers comprising a multivalent N-heterocyclic carbene (NHC) anchoring segment and a functional polymer block were employed as modular surface modifiers (Fig. 1(b)). The NHC units form robust C–Au bonds with adjacent NPs, thereby converting initially noncovalent interparticle junctions into covalently bridged connections without perturbing the predefined spatial geometry. This multivalent anchoring strategy

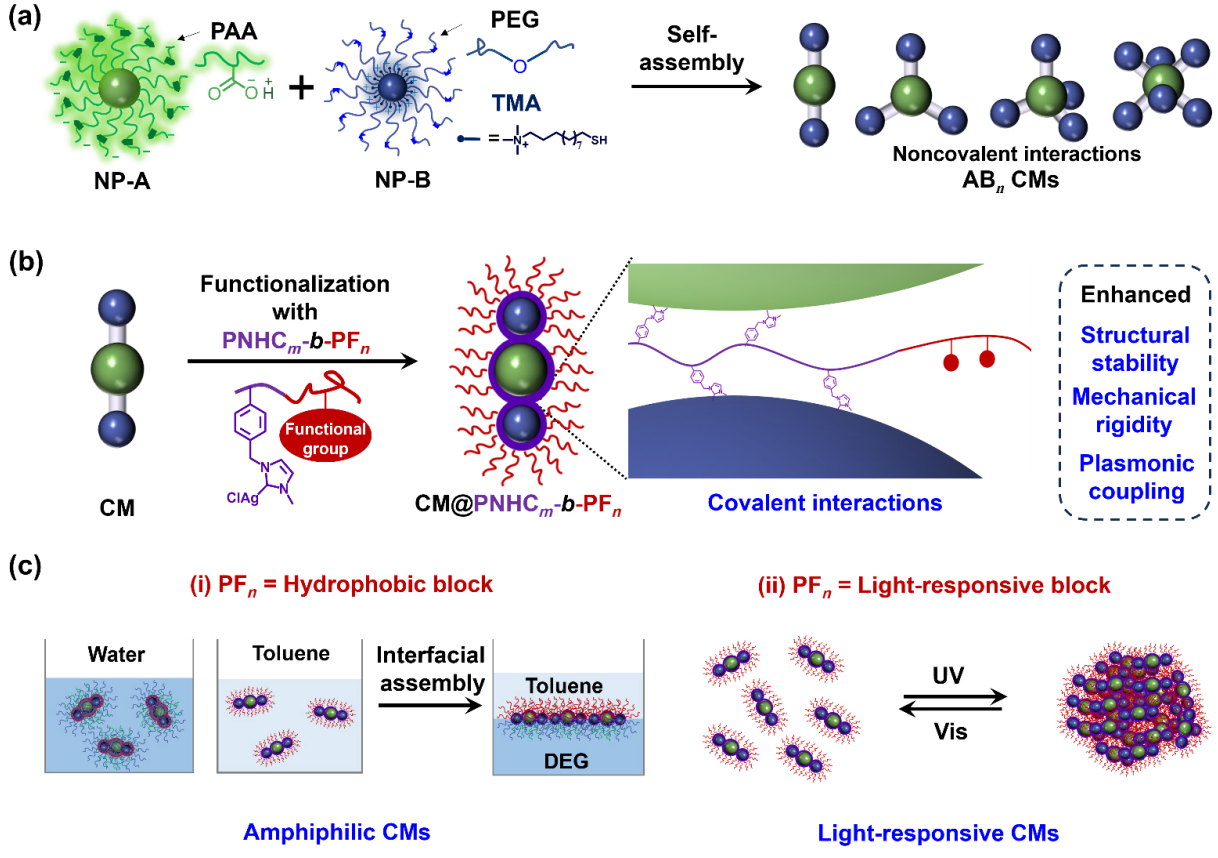

Figure 1 Schematics of the fabrication, functionalization, and hierarchical assembly of CMs. (a) Self-assembly from NPs to AB_n CMs induced by the electrostatic attractions and hydrogen bonds. (b) Post-functionalization from AB_2 CMs to AB_2@PNHC$_m$-*b*-PF$_n$ CMs and the detailed ligand coordination structure between NP-A and NP-B within an AB_2@PNHC$_m$-*b*-PF$_n$ CM. (c) Surface modification of AB_2 CMs by post-functionalization: (i) amphiphilicity and interfacial assembly of AB_2@PNHC$_m$-*b*-PF$_n$ CMs induced by hydrophobic block, and (ii) light-responsive assembly of AB_2@PNHC$_m$-*b*-PF$_n$ CMs induced by light-responsive block.

reduces interparticle spacing and enhances junction rigidity, leading to markedly improved structural robustness under harsh conditions, including strongly acidic (pH 2) and alkaline (pH 12) environments, high salt concentrations (up to 1 M NaCl solution), and elevated temperatures (up to 100 °C), while preserving three-dimensional architectures in the dry state. Importantly, the structural separation between the anchoring block and the functional polymer block enables surface modification independent of structural locking (Fig. 1(c)). By varying the secondary block, amphiphilic and photo-responsive functionalities were incorporated into the covalently stabilized CMs, enabling solvent-dependent plasmonic modulation and light-triggered hierarchical assembly. Our work demonstrates that structural integrity and surface functionality can be independently engineered in discrete NP assemblies through modular post-functionalization.

2 Results and discussion

2.1 Preparation of CMs

CMs serve as an ideal model platform because their discrete and geometrically well-defined architectures, with precisely controlled coordination numbers and symmetry, enable direct structure–property correlations without complications arising from long-range defects [6, 38, 39]. Their interparticle spacing is highly sensitive to external perturbations, allowing subtle structural variations to be amplified into measurable optical responses. Moreover, both the spatial configuration and surface physicochemical properties (e.g., amphiphilicity) of CMs can be readily characterized by electron microscopy and spectroscopic techniques. In this work, CMs with AB_2, AB_3, AB_4, and AB_6 symmetries were prepared via the self-assembly of polymer-grafted Au NPs in aqueous solution. In brief, NP-As were grafted by PAA with strong negative charge, serving as a hydrogen bond donor (Fig. 1(a)). While, NP-Bs were grafted with PEG which served as a hydrogen bond acceptor and provided steric hindrance. The TMA was decorated alongside on NP-Bs to provide weak positive charge. Using a dialysis-mediated strategy to release long-range electrostatic attraction between NP-As and NP-Bs, the PAA ligands on NP-As steadily formed interparticle hydrogen bonds with the PEG ligands on NP-Bs, finally formed AB_n CMs. To obtain different AB_n CMs in high yield, both the molecular weights of the polymers grafted on NP-As and NP-Bs and the diameters of the Au NPs were systematically adjusted according to the target CM geometry. The detailed NP parameters used for CM formation are summarized in Table S1 in the Electronic Supplementary Material (ESM), and representative scanning electron microscopy (SEM) images of AB_2, AB_3, AB_4, and AB_6 CMs are shown in Fig. S1 in the ESM.

2.2 Design and synthesis of multi-nitrogen carbene-containing block polymers

To reinforce the structural integrity of CMs while simultaneously introducing programmable surface functionality, multi-NHC-containing block copolymers were rationally designed for post-functionalization of pre-assembled CMs (Fig. 1(b)). These copolymers comprise two distinct segments: a multivalent NHC anchoring block and a functional polymer block. The NHC moieties were generated *in situ* via deprotonation of imidazolium precursors using the alkalinity of silver oxide (Scheme S4 in the ESM). Subsequently, the resulting NHCs coordinated with silver ions to form stable NHC-Ag complexes, and the presence of Ag in the copolymer was confirmed by X-ray photoelectron spectroscopy (XPS) analysis (Fig. S2 in the ESM). Owing to the strong σ-donating from the lone pair on the carbene carbon and the π-electron stabilization from adjacent nitrogen atoms, NHCs exhibit exceptional affinity toward noble metal surfaces, enabling the formation of robust covalent carbon–metal bonds [40–45]. In this modular design, the multivalent NHC block serves as a strong anchoring segment to secure the copolymer onto Au NP surfaces, while the second polymer block functions as a tunable surface domain. This functional segment allows systematic regulation of CM solubility, surface amphiphilicity, and intermolecular interactions, thereby providing a versatile handle to manipulate interfacial behavior and hierarchical assembly without disrupting the underlying CM architecture (Fig. 1(c)). Based on this design principle, three types of block copolymers were synthesized: (i) diblock copolymers composed of a homopolymeric NHC-containing block and a polystyrene block ($PNHC_n$-*b*-PS_m); (ii) diblock copolymers containing a random NHC/styrene copolymer block and a polystyrene block ($P(NHC_m$-*r*-$St_p)$-*b*-PS_n); and (iii) diblock copolymers composed of an NHC-containing block and a poly(spirobenzopyran methacrylate) block ($PNHC_m$-*b*-$PSPMA_n$). This polymer library enabled systematic control of anchoring density, surface composition, and functional responsiveness.

2.3 Post-functionalization of CMs

The post-functionalization of CMs was carried out by mixing NHC-containing block copolymers with pre-assembled CMs in *N*,*N*-dimethylformamide (DMF) at room temperature. During this process, the multi-NHC block partially displaced the original surface ligands and formed robust C–Au bonds with adjacent NPs (NP-A and NP-B) within individual CMs, thereby reinforcing the interparticle junctions. The evolution of the post-functionalization was monitored *in situ* by ultraviolet–visible (UV–Vis) spectroscopy using AB_2-type CMs modified with $PNHC_9$-*b*-PS_{170} (Fig. 2(a)). The localized surface plasmon resonance (LSPR) peak exhibited a red shift from 533 to 537 nm within the first 2 h (Fig. S3 in the ESM), indicating enhanced interparticle coupling at the early stage of functionalization. From 2 to 72 h, the LSPR band progressively split into transverse and longitudinal modes: The transverse mode blue-shifted from 537 to 531 nm, while a new longitudinal mode gradually emerged at ~ 580 nm. This spectral evolution is characteristic of strengthened plasmonic coupling arising from reduced interparticle separation, suggesting that the multivalent NHC block progressively bridged adjacent nanoparticles and narrowed the A–B gap distance. Cryogenic transmission electron microscopy (cryo-TEM) analysis further confirmed this structural contraction, revealing a decrease in the A–B interparticle distance of AB_2 CMs (Figs. 2(b) and 2(c)), and Figs. S4(a) and S4(b) in the ESM). Importantly, the CM architecture remained intact throughout the process: Both the purity (Fig. S5 in the ESM) and the bond angle distribution (Fig. 2(d)) of AB_2 CMs were almost unchanged before and after functionalization. Consistently, during functionalization, zeta potential measurements showed a transition from −11.8 to +2.3 mV, indicating successful grafting of $PNHC_9$-*b*-PS_{170} onto the CM surface. Additional evidence was provided by XPS: The C 1s spectrum shows a characteristic π–π* shake-up satellite at 291.6 eV (Fig. S6 and Table S3 in the ESM), attributed to the aromatic rings of the polystyrene (PS) block, and a distinct N 1s signal is also observed (Fig. 2(e)). Elemental semi-quantitative

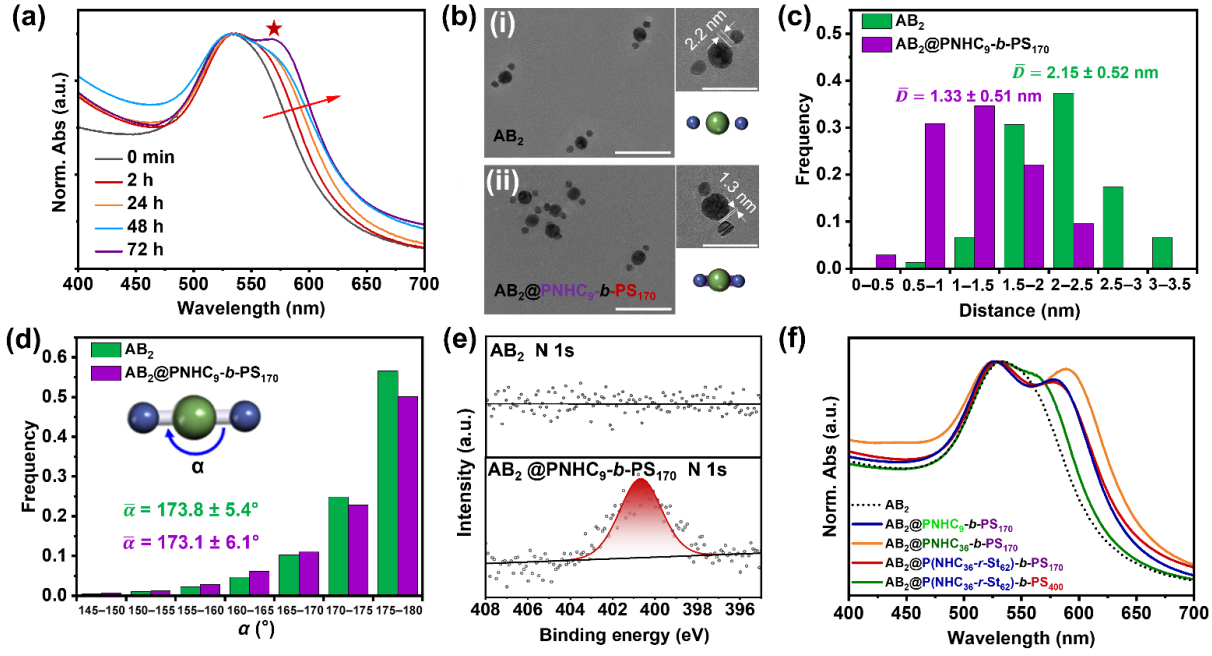

Figure 2 The post-functionalization of AB_2 CMs. (a) Evolution of the UV–Vis absorption spectra during the functionalization of AB_2 CMs with $PNHC_9$-*b*-PS_{170}. (b) Cryo-TEM images of CMs dispersed in water: (i) AB_2 CMs and (ii) AB_2@$PNHC_9$-*b*-PS_{170} CMs. (c) Statistical distribution of the NP-A–NP-B distance in n = 100 AB_2 CMs and n = 100 AB_2@$PNHC_9$-*b*-PS_{170} CMs. (d) Statistical distribution of the bond angle within n = 100 AB_2 CMs and n = 100 AB_2@$PNHC_9$-*b*-PS_{170} CMs. (e) High-resolution N 1s XPS spectrum of AB_2 and AB_2@$PNHC_9$-*b*-PS_{170} CMs. (f) UV–Vis absorption spectra of AB_2 CMs in DMF functionalized by $PNHC_9$-*b*-PS_{170}, $PNHC_{36}$-*b*-PS_{170}, P(NHC_{36}-*r*-St_{62})-*b*-PS_{170}, and P(NHC_{36}-*r*-St_{62})-*b*-PS_{400}.

analysis further shows a pronounced increase in the relative contents of C and N, accompanied by a decrease in O (Table S2 in the ESM). Together, these results confirm the successful covalent anchoring of $PNHC_9$-*b*-PS_{170}, the substitute of the original ligands on CMs, and the associated structural locking of CMs.

2.4 Effect of polymer structure on the post-functionalization

To clarify how polymer architecture of the multi-NHC-containing copolymer influences CM post-functionalization, three structural parameters were systematically varied: (i) the length of the NHC homopolymer block ($PNHC_9$-*b*-PS_{170} vs. $PNHC_{36}$-*b*-PS_{170}); (ii) the distribution of NHC units (homopolymer $PNHC_{36}$-*b*-PS_{170} vs. random copolymer P(NHC_{36}-*r*-St_{62})-*b*-PS_{170}); and (iii) the length of the PS segment (P(NHC_{36}-*r*-St_{62})-*b*-PS_{170} vs. P(NHC_{36}-*r*-St_{62})-*b*-PS_{400}). The corresponding UV–Vis spectra of functionalized AB_2 CMs in DMF are shown in Fig. 2(f), and the elemental semi-quantitative analysis from XPS survey spectra is summarized in Table S2 in the ESM. Extending the NHC homopolymer block induced a clear red shift of the longitudinal LSPR band from 578 ($PNHC_9$-*b*-PS_{170}) to 591 nm ($PNHC_{36}$-*b*-PS_{170}), indicating enhanced plasmonic coupling due to reduced interparticle spacing. Consistently, XPS revealed a sharp increase in the relative contents of N and C, accompanied by a decrease in O. The longer NHC segment provides increased multivalent anchoring, promoting more effective bridging between adjacent nanoparticles. Meanwhile, the increased number of binding sites improves ligand-displacement efficiency, resulting in a higher grafting density of the carbene polymer. When the NHC units were diluted within a random copolymer backbone, the longitudinal peak blue-shifted to 578 nm, compared to 591 nm for the homopolymer analogue. In parallel, the N and C signals decreased markedly and the O content increased. The incorporation of styrene units decreases the spatial continuity of NHC binding sites, decreasing grafting density, lowering bridging efficiency, and weakening coupling. Finally, increasing the PS block length from 170 to 400 nm resulted in attenuation of the longitudinal LSPR mode, together with reduced N and C contents. The longer PS chains introduce greater steric hindrance and reduce effective grafting density, thereby limiting NHC-mediated interparticle contraction. Overall, these results demonstrate that NHC valency, spatial distribution, and secondary block steric effects collectively govern interparticle spacing and plasmonic enhancement in post-functionalized CMs.

2.5 Structural stability of functionalized CMs

In this post-functionalization strategy, the multivalent NHC-containing block is designed to covalently bridge neighboring NP-A and NP-B within each CM, thereby rigidifying the interparticle junctions and enhancing structural robustness. To evaluate the environmental stability of the functionalized assemblies, AB_2@$PNHC_9$-*b*-PS_{170} CMs were subjected to a series of chemical challenges, with unfunctionalized AB_2 CMs examined in parallel as controls. Upon redispersion in aqueous solutions spanning pH 2–12 and standing at room temperature for 4 h, the functionalized CMs retained their well-defined AB_2 configuration across the entire pH range (Figs. 3(a)(v) and 3(a)(vi)). Correspondingly, their UV–Vis spectra preserved the characteristic dual-peak LSPR feature without significant spectral shift (Fig. S7(b) in the ESM), indicating stable interparticle coupling. In contrast, the unfunctionalized AB_2 CMs disassembled under both acidic and alkaline conditions (Figs. 3(a)(i) and 3(a)(ii)), accompanied by a pronounced blue shift of the LSPR peak from 532 to 522 nm (Fig. S7(a) in the ESM), consistent with loss of plasmonic coupling. The robustness of the covalently locked CMs was further confirmed in 1 M NaCl solution. After 4 h of exposure, AB_2@$PNHC_9$-*b*-PS_{170}

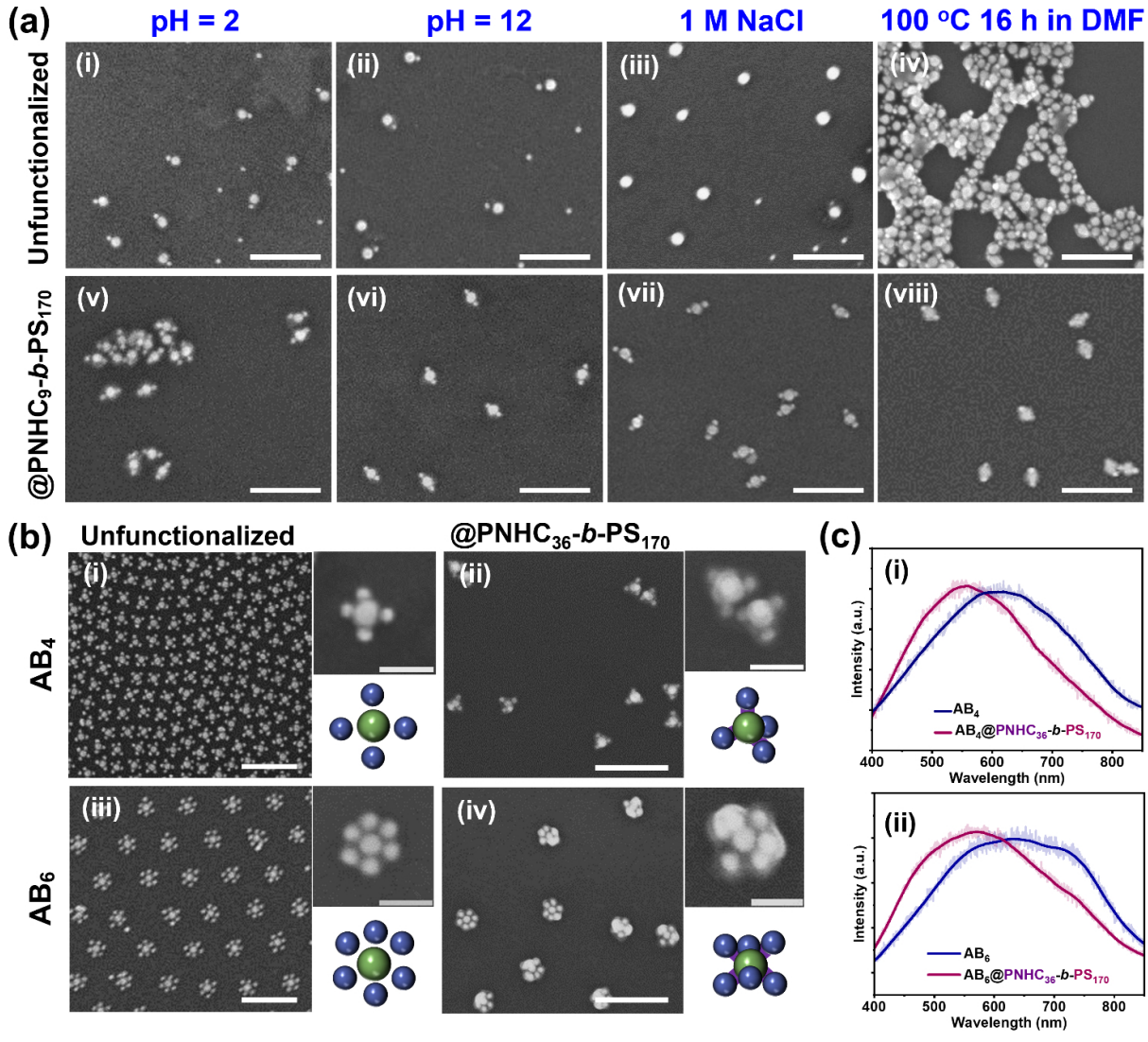

Figure 3 Stability of functionalized CMs. (a) SEM images of CMs in different harsh conditions: (i) AB_2 CMs in aqueous solution at pH 2 for 4 h, (ii) AB_2 CMs in aqueous solution at pH 12 for 4 h, (iii) AB_2 CMs in 1 M NaCl aqueous solution for 4 h, (iv) AB_2 CMs heated at 100 °C for 16 h in DMF, (v) AB_2@$PNHC_9$-*b*-PS_{170} CMs in aqueous solution at pH 2 for 4 h, (vi) AB_2@$PNHC_9$-*b*-PS_{170} CMs in aqueous solution at pH 12 for 4 h, (vii) AB_2@$PNHC_9$-*b*-PS_{170} CMs in 1 M NaCl aqueous solution for 4 h, and (viii) AB_2@$PNHC_9$-*b*-PS_{170} CMs heated at 100 °C for 16 h in DMF. Scale bars are 200 nm. (b) SEM images of CMs dried on the silicon substrate: (i) AB_4 CMs, (ii) AB_4@$PNHC_{36}$-*b*-PS_{170} CMs, (iii) AB_6 CMs, and (iv) AB_6@$PNHC_{36}$-*b*-PS_{170} CMs. Scale bars are 200 nm, and inset scale bars are 50 nm. (c) Dark-field scattering spectra of CMs on silicon substrate: (i) AB_4 CMs and AB_4@$PNHC_{36}$-*b*-PS_{170} CMs, and (ii) AB_6 CMs and AB_6@$PNHC_{36}$-*b*-PS_{170} CMs.

CMs maintained their structural integrity (Fig. 3(a)(vii)), whereas the pristine AB_2 counterparts underwent disassembly (Fig. 3(a)(iii)), highlighting the resistance of the functionalized assemblies to ionic screening and disruption of noncovalent interactions.

The enhanced stability of functionalized CMs was also evident under thermal stress. After heated at 100 °C for 16 h, AB_2@$PNHC_9$-*b*-PS_{170} CMs largely preserved their AB_2 architecture (Fig. 3(a)(viii) and Fig. S8(b) in the ESM), while the pristine AB_2 CMs disassembled under identical conditions (Fig. 3(a)(iv) and Fig. S8(a) in the ESM). Notably, the longitudinal LSPR peak of AB_2@$PNHC_9$-*b*-PS_{170} CMs exhibited a discernible red shift after heating (Fig. S9 in the ESM), suggesting further enhancement of plasmonic coupling. This spectral evolution may arise from partial reorganization or detachment of the original PAA and PEG ligands at elevated temperature, which could expose additional surface sites and enable previously unbound NHC moieties to form secondary coordination across adjacent nanoparticles. Such progressive interparticle bridging would further reduce the NP-A–NP-B gap distance and strengthen coupling. Collectively, these results demonstrate that multivalent NHC anchoring not only stabilizes CM architectures against chemical and ionic perturbations but also reinforces structural integrity under prolonged thermal treatment.

2.6 Mechanical rigidity of functionalized CMs

Following the enhanced chemical and thermal stability discussed above, we next examined whether covalent locking also translates into improved mechanical rigidity of CMs during solvent removal and drying. As shown in Figs. 3(b)(ii) and 3(b)(iv), the functionalized AB_4@$PNHC_{36}$-*b*-PS_{170} CMs and AB_6@$PNHC_{36}$-*b*-PS_{170} CMs largely preserved their tetrahedral and octahedral architectures after deposition and drying on a silicon substrate. This structural retention is attributed to the multivalent NHC block, which forms covalent C–Au linkages that bridge adjacent NP-A and NP-B more tightly and reduce conformational freedom at the

interparticle junctions, thereby resisting deformation during solvent evaporation. Cryo-TEM analysis confirmed that the average NP-A–NP-B distance in AB_4 CMs decreased from 5.5 to 3.3 nm after functionalization (Figs. S4(c) and S4(d) in the ESM). In contrast, the unfunctionalized AB_4 and AB_6 CMs collapsed into two-dimensional planar configurations upon drying (Figs. 3(b)(i) and 3(b)(iii)). Owing to the relatively large interparticle separation and the predominantly noncovalent interparticle connections in the original assemblies, capillary forces generated during solvent evaporation tended to pull the peripheral NP-B units toward the substrate, leading to flattening of the three-dimensional architectures. This distinct morphological evolution is also reflected in the optical response. As shown in the dark-field scattering spectra (Fig. 3(c)), the retained three-dimensional geometry of the functionalized CMs produced stronger local field enhancement on the substrate compared to the collapsed planar structures, resulting in a blue shift of the scattering peak. This behavior is consistent with finite-difference time-domain (FDTD) simulations (Fig. S10 in the ESM), which confirm the geometry-dependent plasmonic response. These results collectively demonstrate that covalent multivalent anchoring transforms mechanically labile supramolecular junctions into rigid interparticle nodes, enabling preservation of 3D geometry.

2.7 Amphiphilicity and interfacial assembly of functionalized CMs

Amphiphilicity plays a central role in nanoparticle assembly and interfacial engineering by enabling adaptive interactions across environments of distinct polarity and facilitating solvent-dependent structural reconfiguration. Although amphiphilic behavior has been widely explored in individual nanoparticles and polymer-coated colloids [46], its integration into discrete and geometrically defined CMs without compromising structural integrity remains largely unexplored. Achieving this capability requires decoupling structural locking from surface reprogramming, thereby allowing assemblies to preserve their architecture while dynamically adapting their interfacial characteristics. In the present system, amphiphilicity was introduced through the rational design of $PNHC_9$-*b*-PS_{170}, in which the NHC block anchors covalently to the gold surface while the PS block functions as a hydrophobic segment. Post-functionalization partially replaced the original PAA and PEG ligands, yielding AB_2@$PNHC_9$-*b*-PS_{170} CMs bearing three chemically distinct polymer domains: PAA, PEG, and PS. The coexistence of hydrophilic (PAA/PEG) and hydrophobic (PS) segments endows the CMs with solvent-adaptive amphiphilicity while maintaining their covalently locked framework. The amphiphilic character of AB_2@$PNHC_9$-*b*-PS_{170} CMs was validated by their stable dispersion across solvents spanning a broad polarity range, from water to toluene, without observable aggregation (Fig. 4(a) and Fig. S11 in the ESM). This solvent tolerance arises from dynamic conformational rearrangement of surface polymer chains (Scheme S10 in the ESM). In a good solvent such as DMF, PAA, PEG, and PS chains adopt extended conformations. In contrast, in toluene, the PS block remains solvated and extended, whereas PAA and PEG segments collapse onto the CM surface. Conversely, in water, PS chains collapse while PAA and PEG remain solvated. These solvent-dependent conformational transitions modulate the effective interparticle environment and influence the NP-A–NP-B separation. Consistent with this structural adaptability, UV–Vis spectroscopy revealed solvent-dependent shifts of the LSPR band (Fig. 4(b)). The most pronounced red shifts were observed in toluene and water, indicating enhanced plasmonic coupling under conditions where selective polymer collapse promotes interparticle contraction. These results demonstrate that solvent-controlled chain reconfiguration enables reversible tuning of interparticle coupling while preserving CM geometry.

Moreover, the solvent-adaptive amphiphilicity of AB_2@$PNHC_9$-*b*-PS_{170} CMs enables directed interfacial assembly. As shown in Fig. 4(d), when a toluene dispersion of AB_2@$PNHC_9$-*b*-PS_{170} CMs was introduced onto a diethylene glycol (DEG) surface, the amphiphilic CMs spontaneously migrated to the toluene–DEG interface and assembled to a monolayer. During evaporation of toluene, the CMs adjusted their assembly configuration consistently at the interface and evolved into a continuous densely monolayer membrane after the evaporation (Figs. 4(c) and 4(e)). The formation of this hierarchical structure was driven primarily by

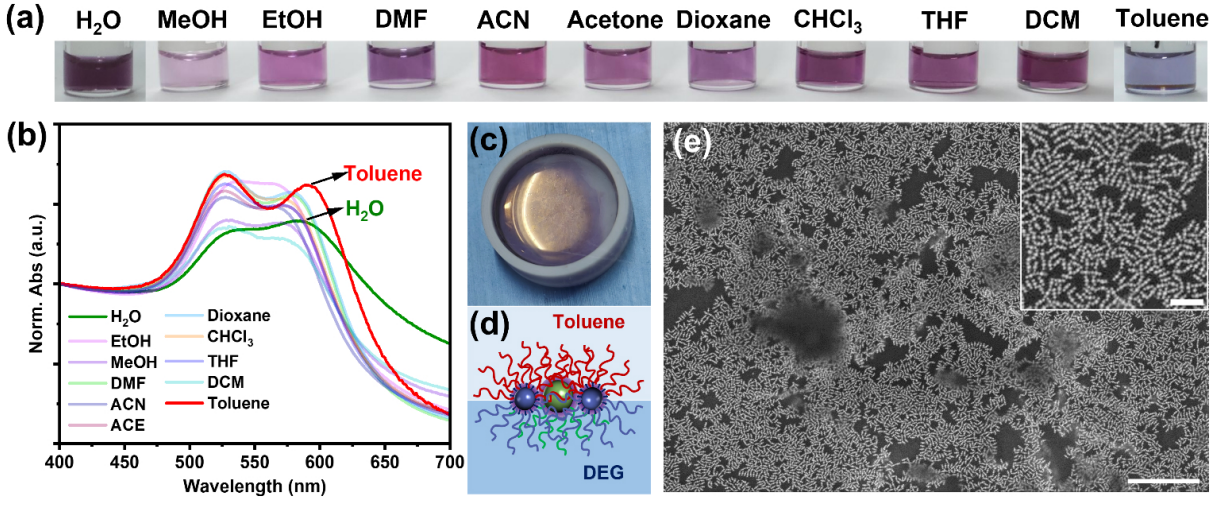

Figure 4 Amphiphilicity and interfacial assembly of functionalized CMs. (a) AB_2@$PNHC_9$-*b*-PS_{170} CMs dispersed in multiple solvents. (b) UV–Vis absorption spectra of AB_2@$PNHC_9$-*b*-PS_{170} CMs dispersed in different solvents. (c) Densely monolayer obtained from interfacial assembly of AB_2@$PNHC_9$-*b*-PS_{170} CMs. (d) The schematic of the ligands conformation on AB_2@$PNHC_9$-*b*-PS_{170} CMs when spreading on the toluene–DEG interface. (e) Large-scale SEM image of the monolayer hierarchical structure. Scale bar is 1 μm, and inset scale bar is 200 nm.

hydrophobic interactions between PS segments, which promoted lateral organization while the covalent NHC anchoring preserved the integrity of individual CMs. Notably, two distinct packing modes, side-by-side and head-to-head configurations, were observed within the monolayer (Fig. 4(e) and Scheme S11 in the ESM), reflecting the anisotropic geometry of the AB_2 building units. These results demonstrate that amphiphilicity not only enables interfacial confinement but also guides orientation-dependent hierarchical assembly, providing a structural basis for constructing ordered CM-based interfacial materials.

2.8 Light-responsive assembly of AB_3@$PNHC_{42}$-*b*-$PSPMA_{42}$ CMs

Building upon the solvent-adaptive amphiphilicity described above, we next investigated whether the surface chemistry of covalently locked CMs could be actively reprogrammed by external stimuli. To this end, a light-responsive block copolymer, $PNHC_{42}$-*b*-$PSPMA_{42}$, was employed to functionalize AB_3 CMs. In this architecture, the multivalent NHC block provides covalent anchoring to preserve structural integrity, while the PSPMA segment introduces light-switchable polarity at the CM surface. As illustrated in Fig. 5(a), spiropyran (SP) units within the PSPMA chains undergo reversible photoisomerization. Upon irradiation at 365 nm, SP converts to the more polar merocyanine (MC) form via ring opening, whereas visible light restores the nonpolar SP state. This SP–MC interconversion modulates surface polarity without perturbing the covalently locked AB_3 framework, thereby enabling surface reconfiguration independent of structural stability. The light-induced assembly behavior was examined using AB_3@$PNHC_{42}$-*b*-$PSPMA_{42}$ CMs dispersed in a toluene/DMF mixture (v/v = 2:1). UV irradiation for 80 min resulted in pronounced aggregation of the CMs, as evidenced by SEM imaging (Figs. 5(d)(i) and 5(b)(ii)). The increased polarity of the MC form enhances electrostatic interactions and π–π stacking among surface-bound chromophores, driving interparticle association. Correspondingly, the in-plane longitudinal LSPR band red-shifted from 576 to 614 nm (Fig. 5(b)), consistent with strengthened plasmonic coupling upon aggregation. The relatively long irradiation time mainly reflects the kinetics of interparticle association in the colloidal system rather than the intrinsic rate of SP photoisomerization [47]. As a control, AB_3@$PNHC_{42}$-*b*-$PSPMA_{42}$ CMs dispersed in toluene/DMF (v/v = 2:1) were heated at 100 °C for 80 min in the dark. In contrast to the pronounced red shift observed after UV irradiation, no red shift of the LSPR band was detected after thermal treatment, indicating that the reversible assembly behavior is not caused by local heating during UV irradiation (Fig. S12(b) in the ESM). Subsequent exposure of the system to visible light for 8 h restored the SP state, leading to redispersion of the assemblies (Fig. 5(d)(iii)). The LSPR peak concomitantly blue-shifted from 614 to 580 nm, indicating recovery of the dispersed state and reduced interparticle coupling. Importantly, the reversibility of this light-responsive process was further confirmed over three consecutive switching cycles, as shown by the reversible UV–Vis peak shifts in Fig. 5(c) and Fig. S12(a) in the ESM. The reversible spectral evolution confirms that light-mediated polarity switching governs interparticle interactions while the NHC anchoring maintains the discrete AB_3 geometry throughout the process. Collectively, these results demonstrate that covalently locked CMs can serve as programmable and stimulus-responsive building units whose surface properties, and consequently hierarchical assembly behavior, can be reversibly controlled without compromising structural definition.

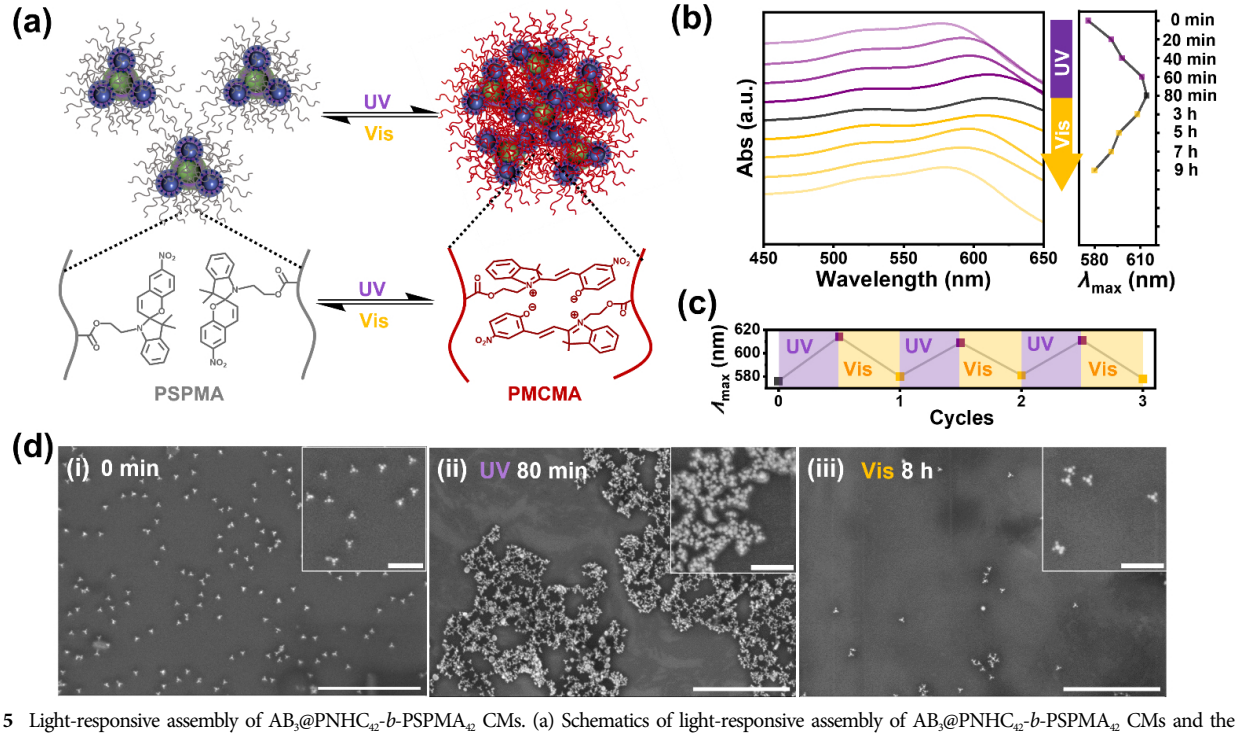

Figure 5 Light-responsive assembly of AB_3@$PNHC_{42}$-*b*-$PSPMA_{42}$ CMs. (a) Schematics of light-responsive assembly of AB_3@$PNHC_{42}$-*b*-$PSPMA_{42}$ CMs and the light-triggered ligand transfer between PSPMA and PMCMA. (b) UV–Vis absorption spectra and peak shifts of AB_3@$PNHC_{42}$-*b*-$PSPMA_{42}$ CMs exposed to 365 nm UV light and visible light for different time in toluene/DMF (v/v = 2:1). (c) Reversible UV–Vis peak-wavelength shifts of AB_3@$PNHC_{42}$-*b*-$PSPMA_{42}$ CMs over three switching cycles under 365 nm UV irradiation (80 min) and visible-light exposure (8 h). (d) SEM images of light-responsive assembly of AB_3@$PNHC_{42}$-*b*-$PSPMA_{42}$ CMs: (i) the initial state, (ii) after exposed to 365 nm UV light for 80 min, and (iii) after exposed to visible light for 8 h. Scale bars are 1 μm, and inset scale bars are 200 nm.

3 Conclusions

In summary, we report a modular post-functionalization strategy that decouples structural locking from surface reprogramming in colloidal molecules. Through multivalent NHC anchoring, initially noncovalent interparticle junctions are converted into covalently bridged connections, affording enhanced chemical, ionic, thermal, and mechanical stability while preserving precise geometric configurations. This covalent locking establishes a robust structural framework that enables subsequent surface modification without compromising architectural integrity. Building on this platform, we demonstrate that CM surface properties can be programmably engineered through rational polymer design. The integration of hydrophilic and hydrophobic segments imparts solvent-adaptive amphiphilicity and interfacial organization, while light-responsive blocks enable reversible and light-directed hierarchical assembly. Notably, these surface transformations occur independently of structural stabilization, underscoring the effective decoupling of geometry and functionality. Collectively, this work elevates colloidal molecules from structurally defined nanoparticle clusters to programmable mesoscale building units with independently tunable stability, interfacial behavior, and responsive assembly. The presented strategy offers a generalizable framework for constructing robust yet reconfigurable nanostructured materials, with broad implications for plasmonics, adaptive interfaces, and stimuli-responsive hierarchical systems.

Electronic Supplementary Material: Supplementary material (the polymer synthetic procedures (Schemes S1–S8), the method for calculating interparticle distances within CMs, the conformations of surface-bound polymers on CMs, and schematic illustrations of hierarchical assembly of CMs (Schemes S9–S11), UV–Vis, SEM, and cryo-TEM characterizations of CMs (Figs. S1–S12), TEM images of NPs (Fig. S13), and ^{1}H NMR spectra of the polymers (Figs. S14 and S15)) is available in the online version of this article at https://doi.org/10.26599/NR.2026.94908810.

Data availability

All data needed to support the conclusions in the paper are presented in the manuscript and the Electronic Supplementary Material. Additional data related to this paper may be requested from the corresponding author upon request.

Acknowledgements

This work was financially supported by the National Natural Science Foundation of China (Nos. 52125308, 52293473, 52433014, 52573292, and 52503074).

Declaration of competing interest

All the contributing authors report no conflict of interests in this work.

Author contribution statement

R. S. Q.: Data curation, project administration, validation, writing manuscript, experimental design. H. N. Z.: Conducting stimulation experiment. J. T.: Experimental design. H. B. H.: Writing manuscript, project administration, experimental design. D. Z.: Writing manuscript, experimental design. W. J. K., Y. L. B., X. Y. Z., and X. Y. H.: Data curation, validation. Y. T. S.: Project administration, writing manuscript, experimental design. Z. H. N.: Project administration, experimental design, funding acquisition. All the authors have approved the final manuscript.

Use of AI statement

None.

References

[1] Yang, F.; Cao, W.; Zheng, G. C.; Qiu, L.; Nie, Z. H.; Li, Y. Plasmonic metasurfaces: Light–matter interactions, fabrication, applications and future outlooks. *Prog. Mater. Sci.* **2025**, *154*, 101508.

[2] Li, Z. W.; Fan, Q. S.; Yin, Y. D. Colloidal self-assembly approaches to smart nanostructured materials. *Chem. Rev.* **2022**, *122*, 4976–5067.

[3] Wu, X. S.; Gao, Y. T.; Wang, H.; Zhang, Z. B.; Xi, X. Y.; Yang, D.; Li, T. T.; Dong, A. G. Hydrophobized metal-organic frameworks as versatile building blocks for tailored nanocrystal superlattices. *J. Am. Chem. Soc.* **2025**, *147*, 6361–6366.

[4] Cao, W.; Tian, S.; Zhong, C.; Qiu, L.; Zeng, P.; Chen, Z. M.; Zhang, X. C.; Liu, H. T.; Liu, K. T.; Li, J. et al. Ultrahigh-resolution nanoimprint patterning of quantum-dot light-emitting diodes via capillary self-assembly. *Nat. Photonics* **2026**, *20*, 301–309.

[5] Nie, Z. H.; Petukhova, A.; Kumacheva, E. Properties and emerging applications of self-assembled structures made from inorganic nanoparticles. *Nat. Nanotechnol.* **2010**, *5*, 15–25.

[6] Yi, C. L.; Liu, H.; Zhang, S. Y.; Yang, Y. Q.; Zhang, Y.; Lu, Z. Y.; Kumacheva, E.; Nie, Z. H. Self-limiting directional nanoparticle bonding governed by reaction stoichiometry. *Science* **2020**, *369*, 1369–1374.

[7] Cui, Y.; Wang, J. C.; Liang, J. C.; Qiu, H. B. Molecular engineering of colloidal atoms. *Small* **2023**, *19*, 2207609.

[8] Cui, Y.; Zhu, H. Y.; Cai, J. D.; Qiu, H. B. Self-regulated co-assembly of soft and hard nanoparticles. *Nat. Commun.* **2021**, *12*, 5682.

[9] He, H. B.; Shen, X. X.; Yao, C. Y.; Tao, J.; Chen, W. W.; Nie, Z. H.; Wu, Y.; Dai, L. W.; Sang, Y. T. Hierarchically responsive alternating nano-copolymers with tailored interparticle bonds. *Angew. Chem., Int. Ed.* **2024**, *63*, e202401828.

[10] Liu, K.; Lukach, A.; Sugikawa, K.; Chung, S.; Vickery, J.; Therien-Aubin, H.; Yang, B.; Rubinstein, M.; Kumacheva, E. Copolymerization of metal nanoparticles: A route to colloidal plasmonic copolymers. *Angew. Chem., Int. Ed.* **2014**, *53*, 2648–2653.

[11] Lu, J.; Xue, Y.; Bernardino, K.; Zhang, N. N.; Gomes, W. R.; Ramesar, N. S.; Liu, S. H.; Hu, Z.; Sun, T. M.; de Moura, A. F. et al. Enhanced optical asymmetry in supramolecular chiroplasmonic assemblies with long-range order. *Science* **2021**, *371*, 1368–1374.

[12] Liu, Y. J.; Li, Y. C.; He, J.; Duelge, K. J.; Lu, Z. Y.; Nie, Z. H. Entropy-driven pattern formation of hybrid vesicular assemblies made from molecular and nanoparticle amphiphiles. *J. Am. Chem. Soc.* **2014**, *136*, 2602–2610.

[13] Song, J. B.; Huang, P.; Duan, H. W.; Chen, X. Y. Plasmonic vesicles of amphiphilic nanocrystals: Optically active multifunctional platform for cancer diagnosis and therapy. *Acc. Chem. Res.* **2015**, *48*, 2506–2515.

[14] Song, J. B.; Zhou, J. J.; Duan, H. W. Self-assembled plasmonic vesicles of SERS-encoded amphiphilic gold nanoparticles for cancer cell targeting and traceable intracellular drug delivery. *J. Am. Chem. Soc.* **2012**, *134*, 13458–13469.

[15] Santos, P. J.; Gabrys, P. A.; Zornberg, L. Z.; Lee, M. S.; Macfarlane, R. J. Macroscopic materials assembled from nanoparticle superlattices. *Nature* **2021**, *591*, 586–591.

[16] Wan, S. Y.; Xia, X. Y.; Gao, Y. T.; Zhang, H. Y.; Zhang, Z. B.; Wu,

F. Y.; Wu, X. S.; Yang, D.; Li, T. T.; Li, J. F. et al. Curvature-guided depletion stabilizes kagome superlattices of nanocrystals. *Science* **2025**, *387*, 978–984.
[17] Wang, Y.; Chen, J.; Zhong, Y. X.; Jeong, S.; Li, R. P.; Ye, X. C. Structural diversity in dimension-controlled assemblies of tetrahedral gold nanocrystals. *J. Am. Chem. Soc.* **2022**, *144*, 13538–13546.
[18] Kim, A.; Kim, C.; Waltmann, T.; Vo, T.; Kim, E. M.; Kim, J.; Shao, Y. T.; Michelson, A.; Crockett, J. R.; Kalutantirige, F. C. et al. Patchy nanoparticles by atomic stencilling. *Nature* **2025**, *646*, 592–600.
[19] Grzelczak, M.; Liz-Marzán, L. M.; Klajn, R. Stimuli-responsive self-assembly of nanoparticles. *Chem. Soc. Rev.* **2019**, *48*, 1342–1361.
[20] Wang, Y.; Chen, G.; Yang, M. X.; Silber, G.; Xing, S. X.; Tan, L. H.; Wang, F.; Feng, Y. H.; Liu, X. G.; Li, S. Z. et al. A systems approach towards the stoichiometry-controlled hetero-assembly of nanoparticles. *Nat. Commun.* **2010**, *1*, 87.
[21] Li, Y. W.; Zhou, W. J.; Tanriover, I.; Hadibrata, W.; Partridge, B. E.; Lin, H. X.; Hu, X. B.; Lee, B.; Liu, J. F.; Dravid, V. P. et al. Open-channel metal particle superlattices. *Nature* **2022**, *611*, 695–701.
[22] Künzle, M.; Eckert, T.; Beck, T. Binary protein crystals for the assembly of inorganic nanoparticle superlattices. *J. Am. Chem. Soc.* **2016**, *138*, 12731–12734.
[23] Yi, C. L.; Zhang, S. Y.; Webb, K. T.; Nie, Z. H. Anisotropic self-assembly of hairy inorganic nanoparticles. *Acc. Chem. Res.* **2017**, *50*, 12–21.
[24] Wang, K.; Ling, H. F.; Bao, Y.; Yang, M. T.; Yang, Y.; Hussain, M.; Wang, H. Y.; Zhang, L. B.; Xie, L. H.; Yi, M. D. et al. A centimeter-scale inorganic nanoparticle superlattice monolayer with non-close-packing and its high performance in memory devices. *Adv. Mater.* **2018**, *30*, 1800595.
[25] He, H. B.; Shen, X. X.; Nie, Z. H. Engineering interactions between nanoparticles using polymers. *Prog. Polym. Sci.* **2023**, *143*, 101710.
[26] Yi, C. L.; Yang, Y. Q.; Liu, B.; He, J.; Nie, Z. H. Polymer-guided assembly of inorganic nanoparticles. *Chem. Soc. Rev.* **2020**, *49*, 465–508.
[27] Santos, P. J.; Cao, Z.; Zhang, J. Y.; Alexander-Katz, A.; Macfarlane, R. J. Dictating nanoparticle assembly via systems-level control of molecular multivalency. *J. Am. Chem. Soc.* **2019**, *141*, 14624–14632.
[28] Hueckel, T.; Hocky, G. M.; Palacci, J.; Sacanna, S. Ionic solids from common colloids. *Nature* **2020**, *580*, 487–490.
[29] Yi, C. L.; Yang, Y. Q.; Nie, Z. H. Alternating copolymerization of inorganic nanoparticles. *J. Am. Chem. Soc.* **2019**, *141*, 7917–7925.
[30] Klinkova, A.; Thérien-Aubin, H.; Choueiri, R. M.; Rubinstein, M.; Kumacheva, E. Colloidal analogs of molecular chain stoppers. *Proc. Natl. Acad. Sci. USA* **2013**, *110*, 18775–18779.
[31] Choueiri, R. M.; Galati, E.; Thérien-Aubin, H.; Klinkova, A.; Larin, E. M.; Querejeta-Fernández, A.; Han, L. L.; Xin, H. L.; Gang, O.; Zhulina, E. B. et al. Surface patterning of nanoparticles with polymer patches. *Nature* **2016**, *538*, 79–83.
[32] Dong, D. S.; Yap, L. W.; Smilgies, D. M.; Si, K. J.; Shi, Q. Q.; Cheng, W. L. Two-dimensional gold trisoctahedron nanoparticle superlattice sheets: Self-assembly, characterization and immunosensing applications. *Nanoscale* **2018**, *10*, 5065–5071.
[33] Zhang, J. Y.; Santos, P. J.; Gabrys, P. A.; Lee, S.; Liu, C.; Macfarlane, R. J. Self-assembling nanocomposite tectons. *J. Am. Chem. Soc.* **2016**, *138*, 16228–16231.
[34] Cai, Y. Y.; Vana, P. 2D plasmonic molecules via hydrogen bond interaction between polymer-grafted nanoparticles. *Angew. Chem., Int. Ed.* **2023**, *62*, e202309798.
[35] Grzelczak, M.; Sánchez-Iglesias, A.; Mezerji, H. H.; Bals, S.; Pérez-Juste, J.; Liz-Marzán, L. M. Steric hindrance induces crosslike self-assembly of gold nanodumbbells. *Nano Lett.* **2012**, *12*, 4380–4384.
[36] Sánchez-Iglesias, A.; Grzelczak, M.; Altantzis, T.; Goris, B.; Pérez-Juste, J.; Bals, S.; Van Tendeloo, G.; Donaldson, S. H.; Chmelka, B. F.; Israelachvili, J. N. et al. Hydrophobic interactions modulate self-assembly of nanoparticles. *ACS Nano* **2012**, *6*, 11059–11065.
[37] Kubiak, J. M.; Macfarlane, R. J. Forming covalent crosslinks between polymer-grafted nanoparticles as a route to highly filled and mechanically robust nanocomposites. *Adv. Funct. Mater.* **2019**, *29*, 1905168.
[38] Shen, X. X.; He, H. B.; Zheng, D.; Cao, W.; Sang, Y. T.; Nie, Z. H. Engineering the electrostatic interactions between oppositely charged polymer-grafted nanoparticles for constructing colloid molecules on substrates. *ACS Nano* **2024**, *18*, 20999–21008.
[39] Wu, Y.; Yang, Y. Q.; Zhang, Y.; Dai, L. W.; Dong, W. H.; He, H. B.; Li, H.; Nie, Z. H.; Sang, Y. T. Photo-induced self-assembly of copolymer-capped nanoparticles into colloidal molecules. *Angew. Chem., Int. Ed.* **2024**, *63*, e202313406.
[40] Tao, J.; Zheng, D.; Tang, Y. T.; He, H. B.; Zhang, Y.; Yang, Y. Q.; Dai, L. W.; Zha, H. N.; Sang, Y. T.; Nie, Z. H. Polymer ligands with multi-nitrogen heterocyclic carbenes for enhanced stability and reactivity in nanoparticle surface functionalization. *Angew. Chem., Int. Ed.* **2025**, *64*, e202419640.
[41] Engel, S.; Fritz, E. C.; Ravoo, B. J. New trends in the functionalization of metallic gold: From organosulfur ligands to N-heterocyclic carbenes. *Chem. Soc. Rev.* **2017**, *46*, 2057–2075.
[42] Hopkinson, M. N.; Richter, C.; Schedler, M.; Glorius, F. An overview of N-heterocyclic carbenes. *Nature* **2014**, *510*, 485–496.
[43] Wei, Z. C.; Mullaj, K.; Price, A.; Wei, K. C.; Luo, Q.; Thanneeru, S.; Sun, S. H.; He, J. Polymer N-heterocyclic carbene (NHC) ligands for silver nanoparticles. *ACS Appl. Mater. Interfaces* **2022**, *14*, 55227–55237.
[44] MacLeod, M. J.; Johnson, J. A. PEGylated N-heterocyclic carbene anchors designed to stabilize gold nanoparticles in biologically relevant media. *J. Am. Chem. Soc.* **2015**, *137*, 7974–7977.
[45] Ferry, A.; Schaepe, K.; Tegeder, P.; Richter, C.; Chepiga, K. M.; Ravoo, B. J.; Glorius, F. Negatively charged N-heterocyclic carbene-stabilized Pd and Au nanoparticles and efficient catalysis in water. *ACS Catal.* **2015**, *5*, 5414–5420.
[46] Hou, S.; Chen, Y. H.; Lu, D. R.; Xiong, Q. R.; Lim, Y.; Duan, H. W. A self-assembled plasmonic substrate for enhanced fluorescence resonance energy transfer. *Adv. Mater.* **2020**, *32*, 1906475.
[47] Siddiqui, K. M.; Bittmann, S. F.; Hayes, S. A.; Krawczyk, K. M.; Sarracini, A.; Corthey, G.; Dsouza, R.; Miller, R. J. D. Ultrafast signatures of merocyanine overcoming steric impedance in crystalline spiropyran. *Nat. Commun.* **2024**, *15*, 10659.